

RESEARCH ARTICLE

10.1029/2017JA025117

Special Section:

Mars Aeronomy

Key Points:

- Overall modeled ion escape and relative contribution of the plume depend on downtail distance
- Acceleration from j times B force appears weaker in simulations when compared to MAVEN data
- Asymmetries in the escape arise from upstream conditions, crustal fields, and neutral atmosphere

Correspondence to:

L. H. Regoli,
lregoli@umich.edu

Citation:

Regoli, L. H., Dong, C., Ma, Y. J., Dubinin, E., Manchester, W. B., Bougher, S. W., & Welling, D. T. (2018). Multispecies and multifluid MHD approaches for the study of ionospheric escape at Mars. *Journal of Geophysical Research: Space Physics*, 123. <https://doi.org/10.1029/2017JA025117>

Received 9 DEC 2017

Accepted 11 AUG 2018

Accepted article online 22 AUG 2018

Multispecies and Multifluid MHD Approaches for the Study of Ionospheric Escape at Mars

L. H. Regoli¹, C. Dong², Y. Ma³, E. Dubinin⁴, W. B. Manchester¹, S. W. Bougher¹, and D. T. Welling¹

¹Climate and Space Sciences and Engineering, University of Michigan, Ann Arbor, MI, USA, ²Astrophysical Sciences and Princeton Plasma Physics Laboratory, Princeton University, Princeton, NJ, USA, ³Institute of Geophysics and Planetary Physics, University of California, Los Angeles, CA, USA, ⁴Max Planck Institute for Solar System Research, Göttingen, Germany

Abstract A detailed model-model comparison between the results provided by a multispecies and a multifluid magnetohydrodynamic (MHD) code for the escape of heavy ions in the Martian-induced magnetosphere is presented. The results from the simulations are analyzed and compared against a statistical analysis of the outflow of heavy ions obtained by the Mars Atmosphere and Volatile EvolutionN/Suprathermal and Thermal Ion Composition instrument over an extended period of time in order to estimate the influence of magnetic forces in the ion escape. Both MHD models are run with the same chemical reactions and ion species in a steady state mode under idealized solar conditions. Apart from being able to reproduce the asymmetries observed in the ion escape, it is found that the multifluid approach provides results that are closer to those inferred from the ion data. It is also found that the $j \times B$ force term is less effective in accelerating the ions in the models when compared with the Mars Atmosphere and Volatile EvolutionN results. Finally, by looking at the contribution of the plume and the ion escape rates at different distances along the tail with the multifluid model, it is also found that the escape of heavy ions has important variabilities along the tail, meaning that the apoapsis of a spacecraft studying atmospheric escape can affect the estimates obtained.

1. Introduction

One of the open questions in relation to Mars is the evolution of its atmosphere. Lammer et al. (2013) provide a multiapproach review on the topic. It is generally accepted that billions of years ago Mars was a warm and wet planet with a significantly thicker atmosphere than found today. Some estimates place the initial surface pressure on the order of tens of bars (e.g., Lunine et al., 2003), a number significantly larger than the less than 10 mbar of the present-day atmosphere. Lacking the shielding effect of a global magnetic field, the atmospheric escape may be particularly significant for nonmagnetized bodies such as Mars (Brain et al., 2016), although this is a current point of debate in the community. Escape can occur in the form of neutrals or ions. In this paper we focus on the latter form, referred to here as ionospheric escape.

The interaction of Mars with the solar wind has been an active subject of study for the space physics community since the first flyby of the planet performed by the Mariner 4 spacecraft in 1965 (Cloutier et al., 1969; Fjeldbo & Eshleman, 1968). After Earth, Mars is the most studied planet in the solar system, with six orbiters and two rovers currently in operation and continuously gathering data for different purposes. One of the most recent missions, MAVEN (Mars Atmosphere and Volatile EvolutionN; Jakosky et al., 2015), has a suite of instruments specifically designed to analyze the different atmospheric escape processes in order to gain insight into the climate evolution of the planet.

Unfortunately, however invaluable the data gathered by the different missions, it is impossible to capture the dynamics of any planetary system at the different spatial and timescales involved with in situ measurements or remote sensing techniques. For this reason, the use of numerical models that combine the theoretical knowledge of the environment being studied with the data collected by spacecraft has become essential. The choice of what model to use is inherent to the physical process one wishes to capture, with the computational effort and the characteristic length scale being the defining factors. A comprehensive review of different models used to study the interaction of Mars with the solar wind can be found in Brain et al. (2010) and Ledvina et al. (2008).

While the computing power is constantly increasing, so is the complexity of several types of models. In terms of magnetospheric dynamics, this has led to the development of different approaches that could be summarized in three main groups: kinetic (particle-in-cell) models (essential when studying small-scale processes that occur at length scales smaller than the electron gyroradius), magnetohydrodynamic (MHD) models (a relatively computationally inexpensive approach to study large-scale structures), and hybrid codes (a combination of the two previous approaches, treating ions as individual particles and electrons as a charge-neutralizing fluid).

Ionospheric escape. Ionospheric escape has been measured by different spacecraft orbiting the planet. The estimates, however, vary significantly among different works, partly due to seasonal effects and solar cycle variations as well as the sensitivity of the results to instrument limitations and the assumptions made to overcome these limitations. These limitations include field of view, uncertainties in the spacecraft charging potential (which affects the ability to measure low-energy populations) and the energy coverage of the instruments that limits the range over which integration of detected fluxes can be made. In addition, prior to MAVEN, no concurrent measurements of plasma and magnetic field data were taken, making it impossible to get information on pitch angle distribution and thus making difficult the interpretation of the overall geometry of the ion escape.

Many authors studied the ionospheric escape from Mars using data from different spacecraft before the arrival of MAVEN (e.g., Barabash et al., 2007; Fränz et al., 2015; Lundin et al., 1990; Verigin et al., 1991), obtaining a wide range of estimates that varies depending on the species included, energy range, and solar conditions. MAVEN arrived at Mars during the unusually weak solar cycle 24, so the escape rates calculated from its instruments are expected to be on the lower side. Nilsson et al. (2011) analyzed more than 4 years of data from the ASPERA-3 instrument for low solar activity, providing a data set that can be contrasted with that collected by MAVEN. The total escape rate found by their study was of $2.0 \pm 0.2 \times 10^{24} \text{ s}^{-1}$. They also analyzed the escape geometry by dividing the escape area along the Y - Z plane (in MSO coordinates with the X axis pointing toward the Sun, the Y axis opposite to the velocity vector of the planet, and the Z axis completing the right-hand triad) and found an asymmetry in the fluxes, with those from the north and dusk quadrants being larger than those from the south and dawn quadrants. The north-south asymmetry was attributed to the presence of the crustal magnetic fields in the southern hemisphere, while the dawn-dusk one was attributed to the asymmetry in the solar wind (Parker spiral).

More recently, using data from the Suprathermal and Thermal Ion Composition (STATIC) instrument on MAVEN (McFadden et al., 2015), Brain et al. (2015) were able to calculate a lower limit for the escape of ions with energies higher than 25 eV at $3 \times 10^{24} \text{ s}^{-1}$. Using the same instrument, Dong et al. (2017) concentrated on the variabilities of the ionospheric plume (a particular escape channel that arises from the acceleration of heavy ions by the solar wind convection electric field) and found that, while the total escape increases from 2 to $3 \times 10^{24} \text{ s}^{-1}$ with increasing extreme ultraviolet (EUV) fluxes for ions with energies higher than 6 eV, the plume remains relatively constant, accounting for 20% to 30% of the total escape.

When compared to previous results, these first estimates based on MAVEN data seem to be significantly lower, something that could be related to the weakness of solar cycle 24 which translates into lower EUV fluxes and, as different authors have pointed out, this leads to lower ionospheric escape (e.g., Dong et al., 2014, 2017; Dubinin et al., 2017; Ramstad et al., 2017). In addition to these cyclical variations, the location where the ions are measured, the energy ranges included in the analyses, and in general the way data are treated differ among the studies and are also a cause of the observed variations that span over 2 orders of magnitude.

The ionospheric escape has also been extensively studied by means of numerical models, including MHD (e.g., Harnett & Winglee, 2006; Holmstrom & Wang, 2015; Ma et al., 2004; Najib et al., 2011) and hybrid (e.g., Bößwetter et al., 2007; Brecht et al., 1993; Kallio et al., 2006; Modolo et al., 2005) codes. Using multispecies MHD simulations, Ma et al. (2004) studied the ionospheric escape taking into account different combinations of solar conditions, interplanetary magnetic field (IMF) configurations, and orientation of the crustal fields. For their case 3 (solar minimum, 3 nT Parker spiral configuration and crustal fields pointing toward the Sun), they estimated the total O^+ ion outflow to be 2.5×10^{23} ions per second, a value that falls on the lower range of the estimates from spacecraft data. They also estimated an outflow of 2.9×10^{23} ions per second for O_2^+ ions. Using a hybrid modeling approach, Modolo et al. (2005) estimated a lower value of O_2^+ escape at 5.0×10^{22} ions per second during solar minimum conditions, although their model did not include the crustal fields and had no ionospheric chemistry. Dong et al. (2014) used a combination of a multifluid MHD model with a

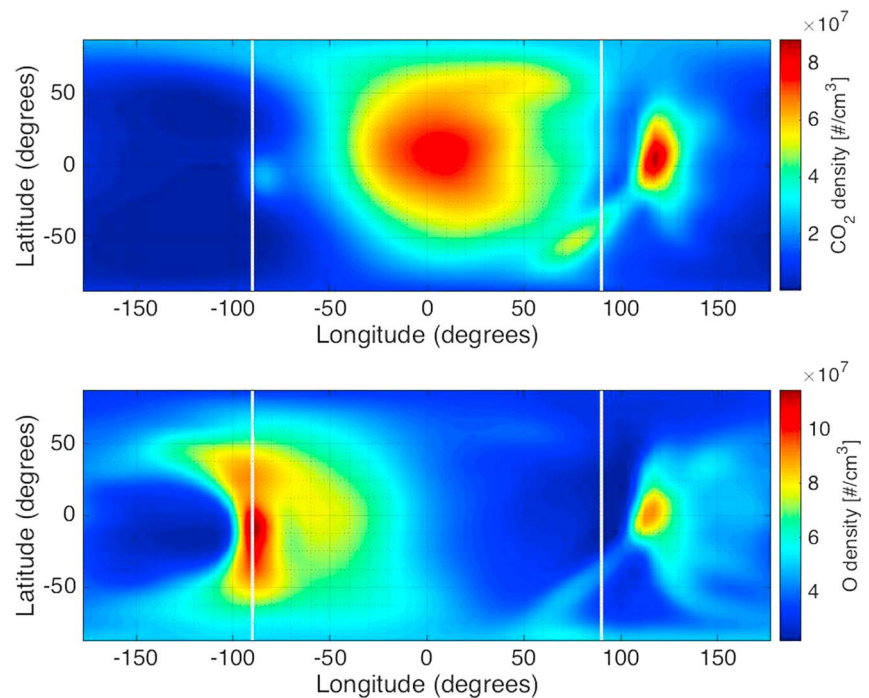


Figure 1. CO₂ (top) and O (bottom) neutral densities at 198.8-km altitude (around the exobase) as calculated by Mars Global Ionosphere-Thermosphere Model. The subsolar point corresponds to a longitude of 0°. The vertical white lines mark the longitude of the terminator line.

3-D atmospheric model to estimate escape fluxes of different species. They found that the inclusion of a 3-D atmospheric model has an important effect in the final estimate of ion outflow. Using the 3-D atmosphere, their estimate of ion outflow was of 4.2×10^{23} ions per second (3.7×10^{24} ions per second) for O⁺ and of 1.7×10^{24} ions per second (2.5×10^{24} ions per second) for O₂⁺ for solar minimum (maximum) conditions and with the crustal fields also pointing toward the Sun.

Also, using a hybrid approach combined with a 3-D model of the atmosphere, Brecht et al. (2016) showed that the inclusion of neutral winds has a noticeable effect on the ionospheric escape by changing the initial energy of the ions being picked up by the solar wind. They calculated the escape values with and without the inclusion of the 3-D neutral winds for different EUV fluxes and found that, at solar minimum fluxes, the total escape rate can vary from $3.1 \times 10^{25} \text{ s}^{-1}$ (without winds) to $4.7 \times 10^{25} \text{ s}^{-1}$ (with winds).

The estimates for ion escape from the multispecies and the multifluid MHD approaches are consistently different from each other. In this paper, we analyze the results provided by a combination of a 3-D model of the neutral atmosphere coupled with a multispecies and a multifluid MHD simulation with the aim of understanding where the differences in escape estimates come from. While the main objective of the study is to provide a model-model comparison, the modeling results are also contrasted with MAVEN observations over an extended period of time in order to understand the effect of magnetic forces in the ion escape and to identify some of the physical processes that are not included in the models and that might be playing an important role in the overall structure of the Martian-induced magnetosphere.

2. Models

For this study, three different models were used in order to provide a fully self-consistent description of the ionospheric escape. The neutral atmosphere was calculated using the Mars Global Ionosphere-Thermosphere Model (M-GITM; Bougher et al., 2015), while two modeling approaches were used for the induced magnetosphere of Mars. These are a single-fluid, multispecies MHD code and a multifluid MHD code, both based on the Block-Adaptive-Tree-Solarwind-Roe-Upwind-Scheme MHD code from the University of Michigan (Powell et al., 1999).

2.1. M-GITM

M-GITM is a 3-D ground-to-exosphere, solar-driven model that uses the monthly averaged F10.7 proxy to self-consistently calculate the atmospheric heating and dynamics. A $1/R^2$ scaling of the corresponding solar EUV-ultraviolet fluxes is applied for the seasonal/heliocentric distance variations of Mars. The code calculates the neutral and ion densities, as well as neutral temperatures and winds. It currently incorporates the main atmospheric constituents, namely, CO_2 , CO , O , N_2 , O_2 , Ar , He , and $\text{N}(4S)$, and the main ionospheric species, namely, O^+ , O_2^+ , CO_2^+ , N_2^+ , and NO^+ . A full set of the chemical reactions included in the code can be found in Bougher et al. (2015).

The code makes use of a spherical grid with fixed latitude and longitude resolution and can work with both a fixed and a stretched vertical resolution. The simulations used in this study were run with an F10.7 value of 110, with a horizontal resolution of 5° by 5° and a fixed vertical resolution of 2.5km . The minimum altitude is the surface ($h = 0\text{ km}$) with no topographic features included and the maximum altitude is 300 km. As a reference, the nominal exobase altitude at Mars is close to 200 km with variations depending on the solar activity (Fox & Hać, 2009). The CO_2 and O densities at 198.8-km altitude (close to the exobase) calculated by M-GITM can be seen in Figure 1. The top panel of the figure shows the concentration of CO_2 close to the dayside where the neutral atmosphere (mostly composed of CO_2) is locally heated while the bottom panel shows the concentration of O that occurs at the nightside due to transport processes that affect the lighter species (Bougher et al., 1999). The regions with enhanced densities in the afternoon sector (longitude $\sim 120^\circ$) appear due to a convergence of the horizontal winds and resulting adiabatic heating in the model.

2.2. Multispecies and Multifluid MHD

The multispecies MHD approach is a step forward from traditional or single-species MHD models that can only solve for the total mass density. In contrast, the multispecies code solves separate continuity equations for each of the included ion species, providing a better description of the mass loading process. The main assumption in this model is that all ions flow with the same velocity so only one momentum and one energy equation are solved. In addition to having the same velocity, all the ion species are assumed to have the same ion temperature, which in turn is assumed to be the same for electrons.

The multifluid MHD contains an extra level of complexity compared to the multispecies approach. In this case, apart from separate continuity equations, each ion has its own momentum and energy equations. This increases the computational effort required to reach a steady state solution, but it allows for the same understanding of the mass loading provided by the multispecies MHD and a better understanding of the ion dynamics.

There are four ions included in both codes, namely, H^+ , O_2^+ , O^+ , and CO_2^+ . The lower boundary of the codes is set to 100 km, meaning that an important overlap exists between M-GITM and the MHD domains. For the overlapping region, the MHD codes take the neutral densities and ionization rates provided by M-GITM to self-consistently calculate the ionosphere of the planet by means of 10 different photochemical and ion-neutral reactions.

The limits of the simulation domain are the same for both approaches and are defined, in Mars radii ($1R_M = 3396\text{ km}$), as -24 to $8R_M$ in the X direction and -16 to $16R_M$ in the Y and Z directions. The models make use of a stretched spherical grid starting at an altitude of 100 km with a 16-km resolution. This provides enough volume to calculate the flow of ions along the tail as well as sufficient space upstream of the planet for the generation of the bow shock. The codes make use of the adaptive mesh refinement technique and are parallelized in order to allow for a fast convergence to a steady state solution. While the codes can be run in time-dependent mode as well, this feature is useful when introducing time-dependent changes in the boundary conditions and thus is not used in this study.

The codes also contain a description of the crustal magnetic fields of Mars in the form of a 60° harmonic expansion that was first described by Arkani-Hamed (2001). While the specific azimuthal location of the crustal magnetic field has been recently shown to affect the magnetospheric dynamics at Mars (e.g., Dong et al., 2015; Fang et al., 2017; Ma et al., 2014), for this study we set the main magnetic anomalies on the nightside. Given that both models are run under the same conditions and that the spacecraft data used covers an extended period of time, the variations arising from crustal field orientation will be smoothed out, so this is not expected to have significant results when performing our comparisons.

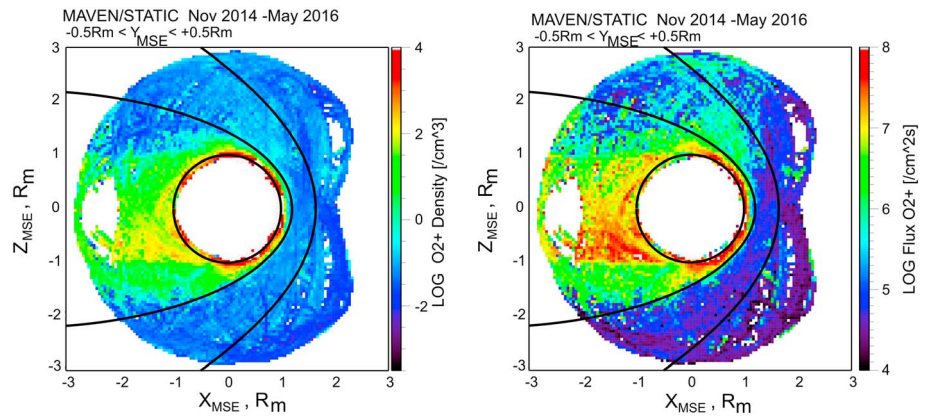


Figure 2. O_2^+ densities (left panel) and fluxes (right panel) in the XZ plane in MSE coordinates calculated using data from the STATIC instrument. MAVEN = Mars Atmosphere and Volatile Evolution; STATIC = Suprathermal and Thermal Ion Composition.

While both codes have been shown useful to study different aspects of the interaction, when it comes to estimating the outflow of ions, the results differ consistently by a factor of about 5 to 6 (e.g., Dong et al., 2014), with the multifluid providing higher estimates than the multispecies. Moreover, each code has been applied to study different aspects of the interaction, but no dedicated comparison has been made to evaluate in a macroscopic sense the effect that solving a different set of equations for each model has in the ionospheric escape beyond comparing ionospheric escape rates (e.g., Dong et al., 2014; Najib et al., 2011).

In this paper, we use ion escape data collected by the MAVEN spacecraft to compare with the output of each of the models. The aim of the study, however, is not to benchmark the performance of each code in a traditional along-the-track comparison, but to investigate the reasons behind the difference in the results provided by each code.

3. Ion Escape as Detected by MAVEN

In order to provide a comprehensive picture of the ionospheric escape, data collected between November 2014 and May 2016 by the STATIC instrument aboard the MAVEN spacecraft were used. The orbital coverage achieved by MAVEN during this period allows for a statistically significant result against which modeling results can be contrasted. The STATIC instrument was designed to measure ion fluxes and composition in the energy range between 0.1 eV and 30 keV and it can resolve the major ion species present at Mars. This energy range is, however, affected by the spacecraft charging and velocity, making it difficult to estimate the escape rates at the lowest energies, in general, leading to an underestimation of the total fluxes.

The outflow of O_2^+ ions was calculated using data from the STATIC instrument onboard MAVEN. The data used were collected between 1 November 2014 and 15 May 2016. Corrections related to the spacecraft velocity and the spacecraft potential (provided by STATIC as a data product at low altitudes when the potential is negative) were applied calculating the ion distribution functions. For the calculations, mean fluxes of ions in each bin in the YZ cross section at tail distances between $-2R_M < X < -1R_M$ were multiplied by the area and summed. Standard deviations of ion fluxes in different energy ranges and for different solar wind conditions can be found in Dubinin et al. (2017). The fluxes were transformed to MSE coordinates system (Z axis aligned with the positive direction of the solar wind convection electric field, the X axis pointing toward the Sun and the Y axis completing the right-hand triad) by using 30-min-averaged data from the MAG instrument for each MAVEN orbit.

The composite averages of the density (left panel) and ion outward fluxes (right panel) in the XZ plane in MSE coordinates are shown in Figure 2. This coordinate system makes it possible to better study the geometry of the heavy ion escape, largely affected by the acceleration of particles by the local electric field. Positions of the nominal boundaries of the bow shock and the induced magnetosphere (Dubinin et al., 2006) are also given.

Here the asymmetry in the fluxes caused by the direction of the solar wind motional electric field is clearly observed in the right panel. In the regions outside of the induced magnetospheric boundary the O_2^+ fluxes dominate in the $E+$ hemisphere, directed along the $+Z$ axis. In contrast, within the Martian magnetosphere

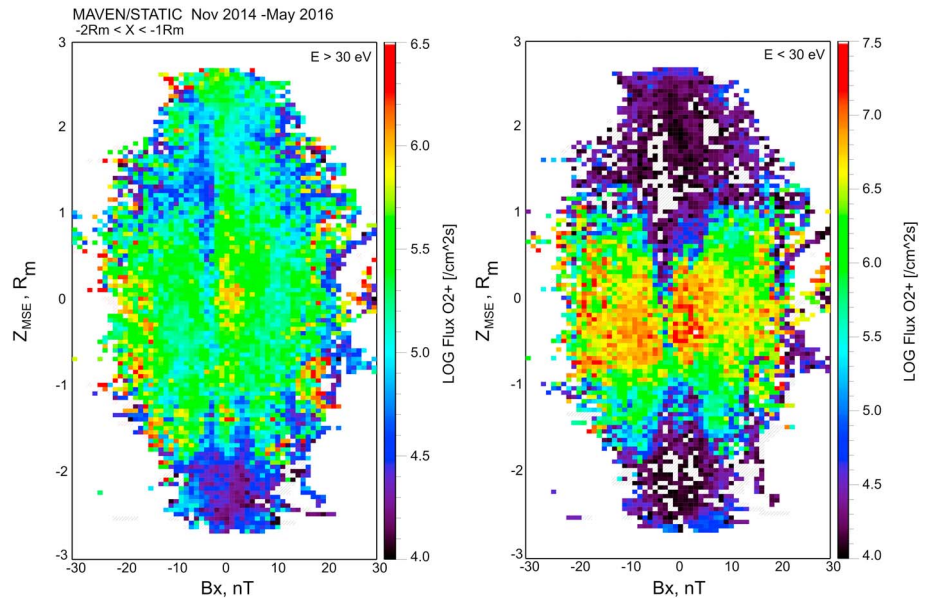


Figure 3. O_2^+ fluxes in the Martian tail measured by the STATIC instrument. The vertical axis corresponds to the Z axis while the horizontal axis corresponds to the magnetic field as measured by the MAG instrument at distances along the X axis between -2 and $-1R_M$. MAVEN = Mars Atmosphere and Volatile Evolution; STATIC = Suprathermal and Thermal Ion Composition.

we observe a shift of the O_2^+ ion population toward the opposite $E-$ hemisphere. A sharp drop of fluxes at the border of the wake appears due to a negative spacecraft potential in the shadow which improves the sensitivity of STATIC to detect cold ionospheric ions. It is seen that, along the tail, the escape ion fluxes are dominant in the $E-$ hemisphere.

Figure 3 shows maps of O_2^+ fluxes in the tail in a modified MSE coordinate system. The vertical axis corresponds to the Z axis while the horizontal one corresponds to the magnetic field as measured by the MAG instrument at distances along the X axis between -2 and $-1R_M$. This coordinate system allows for a better separation of the regions occupied by the planetary ions of different origin (Dubinin et al., 2017).

The left (right) panel shows the fluxes of ions with energy above (below) 30 eV. Ions with higher energy are mostly observed in the plasma sheet centered at the reversal of the B_x component. These ions are accelerated by the $j \times B$ force related to the strong magnetic tensions of the draped magnetic field lines (Dubinin et al., 2012). Another energized ion component is observed at the flanks of the induced magnetosphere and is originated in the boundary layer. Low-energy ions occupy the tail lobes. It is also seen that the major ion losses occur in the low-energy component.

Calculating the O_2^+ ion escape along the tail using STATIC data, we estimate a total flux of about $3.5 \times 10^{24} s^{-1}$ between -1 and $-2R_M$ and about $3.85 \times 10^{24} s^{-1}$ between -2 and $-3R_M$ respectively, with losses varying by up to a factor of 6 – 8. These calculations do not include any fluxes outside the induced magnetosphere and are also constrained in energy range due to spacecraft charging issues. This estimate of the total flux

Table 1
Solar Wind Conditions Used as Input for the Simulations

Solar wind condition	Value
H^+ density	4.00 cm^{-3}
H^+ temperature	15.08 eV
H^+ velocity (magnitude)	400.00 km/s
Magnetic field magnitude	3.00 nT (Parker spiral)
Magnetic field vector	(-1.68, 2.49, 0) nT
Solar wind dynamic pressure	1.3092 nPa

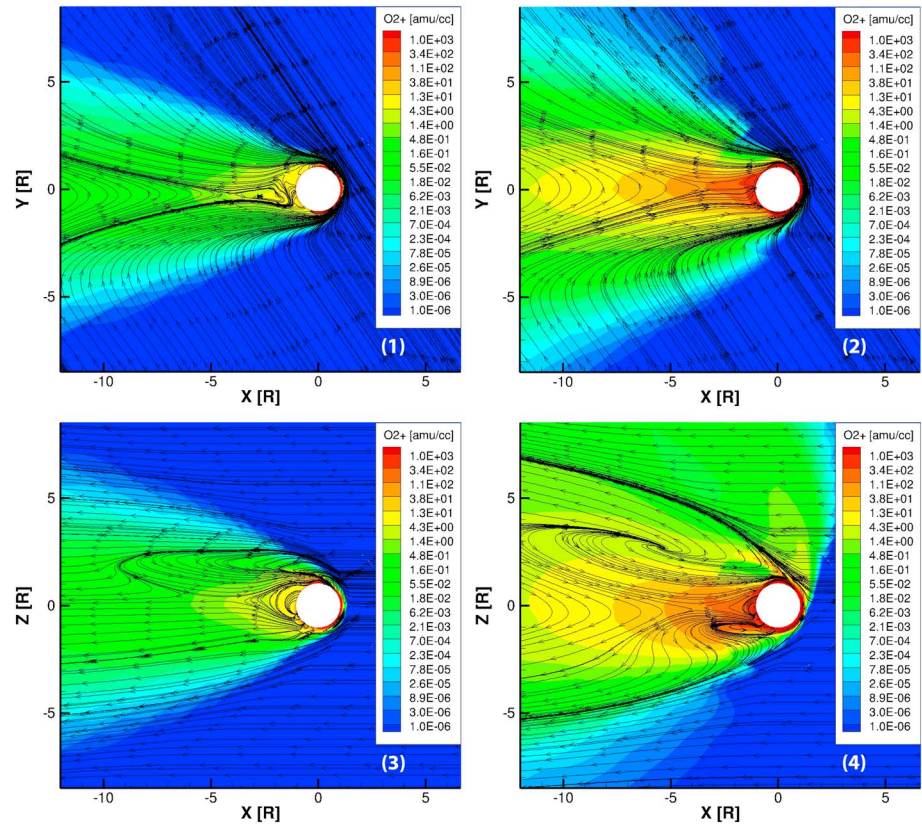


Figure 4. O_2^+ densities around Mars as calculated with a multispecies (left column) and multifluid (right column) magnetohydrodynamic code for solar wind conditions corresponding to a 3-nT Parker spiral. The top panels (1 and 2) show the XY plane, and the bottom panels (3 and 4) show the XZ plane in MSO coordinates. The stream traces represent projections of the magnetic field lines in the respective plane and are a combination of interplanetary magnetic field and crustal fields close to the planet.

is comparable to the $3 \times 10^{24} \text{ s}^{-1}$ reported by Brain et al. (2015) using measurements taken by the same instrument on the MAVEN spacecraft at a spherical shell located at 1,000-km altitude.

4. Ion Escape as Estimated by the Models

For the estimation of ion outflow from the planet, both models were run under idealized solar wind conditions as shown in Table 1 and using the output of M-GITM, run for $L_s = 0$, taking into account the tilt of the planet. Both models were run under steady state conditions for 50,000 iterations until the output was stable and the results for the last iteration are shown in Figure 4. The left-hand panels show the density of O_2^+ ions from the multispecies code while the right-hand panels show the same parameter from the multifluid code.

The overall topology differs significantly between both models, with the multifluid code being able to capture the asymmetries in the outflow that arise from the initial acceleration of the heavy ions provided by the local electric field. Since during the simulations the solar wind convection electric field points toward the north of the planet, ions that are picked up in the southern hemisphere are accelerated toward the planet itself being lost to the atmosphere while ions that are picked up in the northern hemisphere are able to escape the near-Mars environment in the form of a plume. These asymmetries have been reported in previous multifluid MHD simulation results (Dong et al., 2014; Najib et al., 2011). In terms of observations, the presence of plume-like distributions has been reported for escaping O^+ by Dong et al. (2015). They reported that the plume is a constant structure, indicating that in order to properly study the geometry of the escaping fluxes with fluid models, a multifluid approach is necessary.

While the asymmetry in the escape pattern is only observed with the inclusion of different ion fluids in the simulations, this does not directly imply that the total escaping fluxes will be better estimated by the use of a multifluid approach. For this reason, the total escaping flux of ions passing through a spherical shell located sufficiently far from the planet is calculated. Here we take the value of $6R_M$ that was adopted in the study by

Table 2
Calculated Outflow (in s^{-1}) by the MHD Models for Three Different Ion Species

Species	MS-MHD	MF-MHD	Ratio (MF/MS)
O^+	7.00×10^{23}	1.03×10^{24}	1.48
O_2^+	2.13×10^{24}	9.03×10^{24}	4.23
CO_2^+	1.88×10^{23}	9.56×10^{23}	5.07

Note. MS = multispecies; MF = multifluid; MHD = magnetohydrodynamic.

Dong et al. (2014), so the outward fluxes are calculated at a spherical shell located at that distance from the center of the planet. The values obtained by each model for the three ion species considered are shown in Table 2.

The ratios listed in the last column of Table 2 are in good agreement with the results reported in Dong et al. (2014), with differences within 50% for O^+ and O_2^+ and a factor of 2.5 for CO_2^+ . In terms of total heavy ion escape (O^+ , O_2^+ , and CO_2^+), the multispecies gives a value of $3.02 \times 10^{24} s^{-1}$ while the multifluid gives a value of $1.10 \times 10^{25} s^{-1}$. This compares to 2.4×10^{24} and $6.6 \times 10^{24} s^{-1}$ for the multispecies and multifluid, respectively, from Dong et al., (2014; the ; Dong et al., 2014, simulations were run with slightly different solar conditions).

Apart from the monotonically increasing difference with ion mass, the geometry of the escape differs significantly between both models. Figure 5 shows the escaping O_2^+ fluxes at an altitude of $6R_M$ as estimated by the multispecies (top) and multifluid (bottom) MHD simulations. The panels show an equirectangular projection of the spherical shell showing the logarithm of the outward fluxes to better resolve small scales. All the inward fluxes, which would correspond to negative values, are represented as white regions, irrespective of their magnitude.

The asymmetry and the presence of different escape channels for the heavy ions is clearly visible in the multifluid plots from Figure 5. While the escaping flux is concentrated at the center of the tail in the case of the multispecies model, there is a clear asymmetry present in the case of the multifluid that arises, as already mentioned, from the direction of the solar wind convection electric field, pointing in the +Z direction. Also visible is the extended region that is made available for the escaping ions in the case of the multifluid compared to the multispecies, something that ultimately leads to an increase in the escaping fluxes estimated, something that can be observed with the relative contribution of the plume to the total escape, presented toward the end of this section.

Apart from the north-south asymmetry, there are two dawn-dusk asymmetries visible in the case of the multifluid MHD. There is an outward flux of ions at low latitudes, but its magnitude, at about 10 orders of magnitude lower than the highest fluxes, is negligible. The other asymmetry is more prominent, with an overall dawnward enhancement of the escape starting almost at the equator and being significantly pronounced at higher latitudes. This enhanced escape arises from three factors. The first one is the enhancement in the neutral oxygen present close to the dawn terminator region visible in Figure 1 that is the main source of O_2^+ ions through the chemical reaction shown in equation (1).



The other two factors are the presence of the crustal magnetic fields (in the nightside during the simulation) and the B_x component of the IMF. Figure 6 shows the relative effect of these factors in the observed dawn-dusk asymmetry.

Figure 6a shows the same escaping fluxes of O_2^+ ions presented in Figure 5. For Figure 6b, the crustal fields have been disabled in the simulation. For Figure 6c, the crustal fields are disabled, and a spherically symmetric

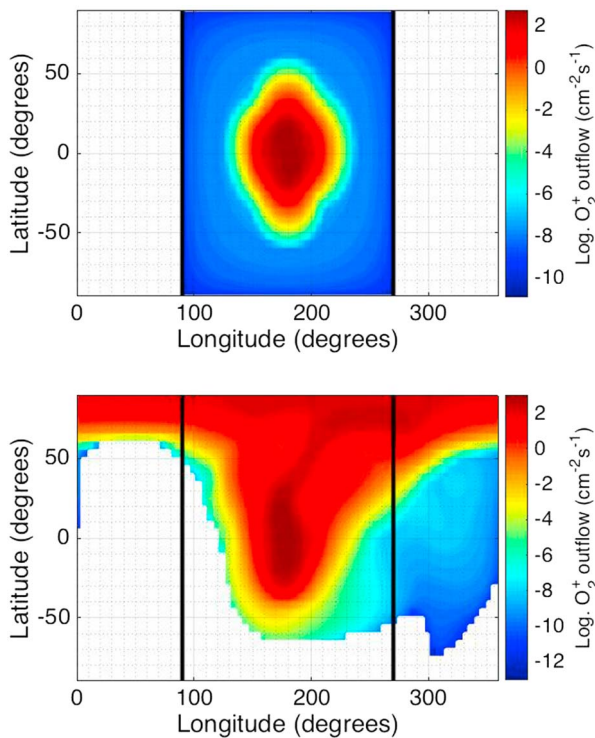


Figure 5. Outward O_2^+ fluxes at an altitude of $6R_M$ as estimated by the multispecies (top) and multifluid (bottom) magnetohydrodynamic simulations. The vertical black lines in the right panels mark the longitude of the terminator line.

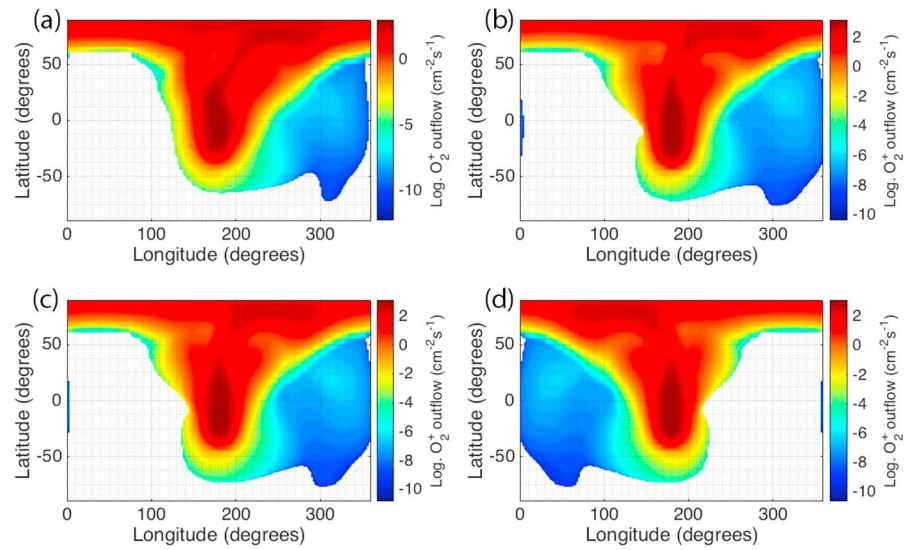


Figure 6. Outward O_2^+ fluxes at an altitude of $6R_M$ as estimated by the multifluid magnetohydrodynamic simulations under the same conditions as those used for Figure 5 (a); without crustal fields (b); without crustal fields and with a symmetric atmosphere (c); and without crustal fields, with a symmetric atmosphere, and with inverted interplanetary magnetic field (d).

atmosphere is used. Finally, for Figure 6d, the crustal fields are disabled, a symmetric atmosphere is used, and the direction of the IMF is inverted along the X direction.

From a direct comparison between the escape geometry from the four individual panels of Figure 6, it is evident that the most important factor in controlling the dawn-dusk asymmetry of the escape is the IMF direction. The presence of the crustal fields has also an appreciable effect, especially at low latitudes, where the area for escaping ions becomes narrower (notice, for instance, the small bite-out close to the equator at a longitude of about 130°) and also in the orientation of the current sheet at midlatitudes (at around 50°). The asymmetries in the neutral atmosphere, however, seems to have a negligible effect, indicating that the dynamics of the system are more important than the source of the ions when it comes to defining the magnetic topology and the overall escape geometry.

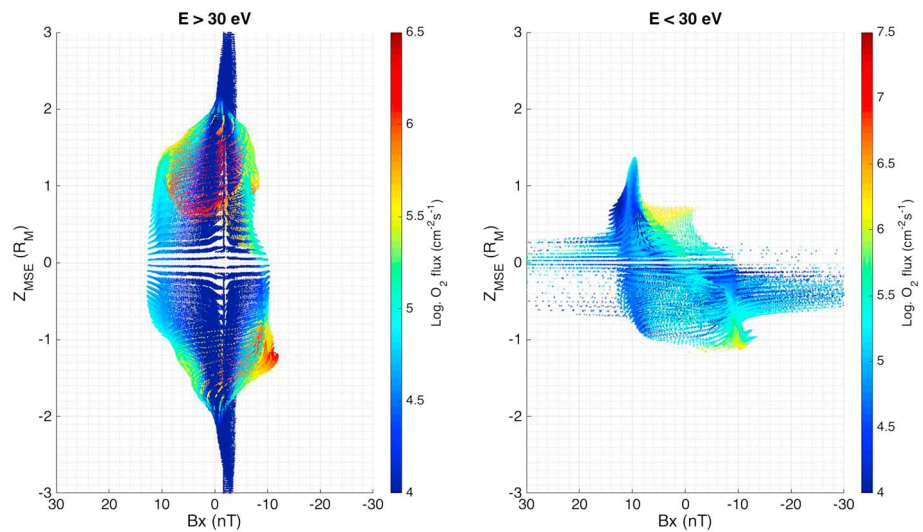


Figure 7. Modeled O_2^+ fluxes in the Martian tail using the multispecies approach. The vertical axis corresponds to the Z axis, while the horizontal axis corresponds to the B_x component of the magnetic field at distances along the X axis between -2 and $-1R_M$. The left panel shows high-energy ($E > 30$ eV) and the right panel low-energy ($E < 30$ eV) ions.

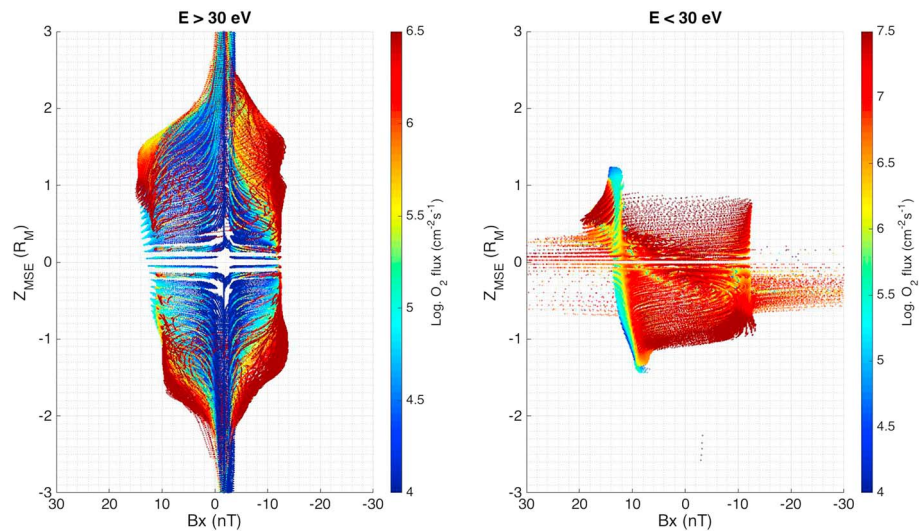


Figure 8. Modeled O_2^+ fluxes in the Martian tail using the multifluid approach. The vertical axis corresponds to the Z axis while the horizontal axis corresponds to the B_x component of the magnetic field at distances along the X axis between -2 and $-1R_M$. The left panel shows high-energy ($E > 30$ eV) and the right panel low-energy ($E < 30$ eV) ions.

Magnetic forces. Similar to the plots from Figure 3, visualizing the ion escape as a function of the magnetic field along the tail (B_x) provides insight on the effect that magnetic forces have on the escaping particles. In order to provide a comparison to the plots shown in Figure 3, where two energy ranges were shown, Figures 7 and 8 show the outflow of O_2^+ for the multispecies and multifluid models respectively at the same distances along the tail, divided by the same energy range used for the data analysis.

There are some similarities and some differences between the simulation results and those obtained by the integration of data from the STATIC instrument. As stated toward the end of section 3, there seems to be a difference between the escape path for low-energy ($E < 30$ eV) and high-energy ($E > 30$ eV) ions. While high-energy ions can be mostly found at the center of the current sheet and at the flanks of the induced magnetosphere, low-energy ions are mostly concentrated at the lobes. This pattern is visible in the simulations, although with a strong dependence on the distance from the equator that is not as clear in the data. In addition, the high-energy population at the center of the simulated current sheet does not appear to be as strong.

The fact that, at least close to the equator, the main population at the center of the current sheet consists of low-energy ions seems to indicate that the acceleration leading to the high-energy component observed in the STATIC data might be due to a process not included in the models such as magnetic reconnection, or simply that the draping of the field lines in the model is not as strong, leading to a weaker energization by the $j \times B$ term. While different signatures of magnetic reconnection at Mars have been observed (e.g., Brain et al., 2007; Eastwood et al., 2008; Halekas et al., 2009; Harada, et al., 2015a), the short distances at which MAVEN is sampling means that the reconnection point is tailward from the spacecraft.

One thing to notice is the acceleration at the center of the current sheet above and below the planet. Given the steady state nature of the simulations, the IMF field lines that are draped around the planet might not have an efficient way to be transported toward the tail, and hence, the slingshot effect arising from the $j \times B$ force is not as effective at low latitudes as it is at high latitudes. A detailed analysis of the $j \times B$ force term comparing a subset of orbits with similar solar wind and IMF conditions with tailored time-dependent simulations is necessary in order to quantify this effect.

Relative contribution of the plume escape. Using the multifluid approach, it is possible to examine the relative contribution of the plume to the total ionospheric escape, similar to the analysis carried out by Dong et al. (2017). In their study, they used integration areas defined as $x > 1.6R_M$ and $\sqrt{x^2 + y^2} \leq 2.5R_M$ for the plume

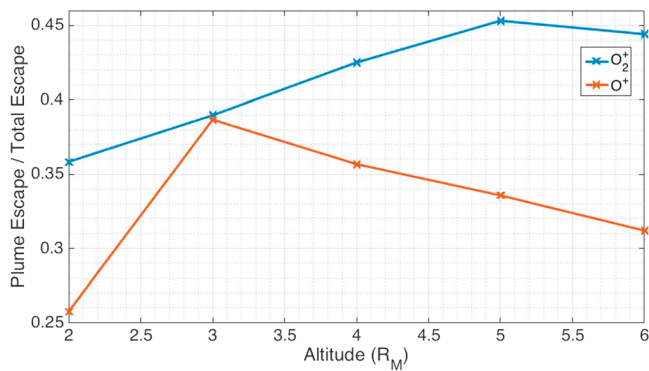


Figure 9. Relative contribution of the plume escape to the total O_2^+ and O^+ escape with respect to altitude.

and $z < 1.6R_M$ and $\sqrt{y^2 + z^2} \leq 2.5R_M$ for the tail. With this definition, they found that, under normal EUV conditions, the plume accounts for about 30% of the total escape, a value that is likely to be energy dependent as well.

The calculations are constrained by the relatively low apoapsis of MAVEN. With the advantage of an extended coverage with the global MHD model, we are able to estimate the evolution of this proportion, with the understanding that the further downstream the calculation is made, the more mixed the plasma from both sources (i.e., tail and plume) will be. In order to do this, we get rid of the cylindrical constraints from Dong et al. (2017) and use instead a constraint defined by latitude. We then take all the escape at latitude angles larger than 50° to correspond to plume escape, with the rest corresponding to escape along the tail. We repeat the calculation for altitudes between 2 and $6R_M$ and the results are shown in Figure 9.

The plot shows the relative contribution for O_2^+ and for O^+ escape. Although throughout the paper we have focused mostly on O_2^+ as the main escaping ion, the results from Figure 9 will be analyzed focusing on O^+ , since that is the ion that was studied by Dong et al. (2017). From the plot it can be seen that the relative contribution estimated by the multifluid MHD model at the same radial distance used for the Dong et al. (2017) analysis ($2.5R_M$) is in very good agreement with that derived from the data, being a factor of 1.07 (33% for the model vs. 30% for the data). The plot also shows that the relative contribution reaches a maximum at around $3R_M$, where the plume accounts for 38% of the total escape. At larger distances, the relative contribution decreases, probably due to way the plume/tail boundary is defined. Taking a constant angle means that with increasing distance from the planet, at some point the plume ions being convected downstream will enter the region defined as the tail.

The situation is similar when looking at the relative contribution for O_2^+ escape, only that the maximum is reached at a distance of $5R_M$. The reason for this lies in the asymmetric acceleration of ions with different masses, with the heavier ones having larger momentum and thus traveling farther from the planet before crossing the arbitrary boundary dividing the two regions, as already described.

5. Discussion

One of the main uncertainties present for data analysis studies is spacecraft charging. When the spacecraft is illuminated by sunlight it acquires a negative charge that causes ions of low energies to be repelled. This prevents the instruments from measuring ions with energies below the charging potential. This means that the detected fluxes will change depending on the location of the spacecraft and will be larger in the wake, where the potential becomes positive. Taking a simple ratio of the areas covered by the spacecraft during an orbit, this translates into an underestimation of the fluxes by up to a factor of 4.

During normal solar wind conditions and the solar EUV value adopted in this study, the dominating escaping ion is O_2^+ and that is why we chose this ion species as a starting point. Using data from the STATIC instrument over a period between November 2014 and May 2016, we estimated an ion outflow of $\sim 3.85 \times 10^{24} \text{ s}^{-1}$

at a distance between -2 and $-3R_M$. When looking at the model results, using the multispecies model we estimated an outflow of $2.13 \times 10^{24} \text{ s}^{-1}$ while with the multifluid the number increases to $9.03 \times 10^{24} \text{ s}^{-1}$.

These numbers are, however, calculated at a larger distance, specifically at $6R_M$. If the outflow is calculated at $3R_M$, the numbers decrease to $2.05 \times 10^{24} \text{ s}^{-1}$ for the multispecies model and to $8.42 \times 10^{24} \text{ s}^{-1}$ for the multifluid. The reason for this variation is that the ions escaping have different velocities and part of the flow can be reflected in the complex field topology present at the tail. This means that the outflow will only be stabilized at a certain distance from the planet. This effect, shown in Figure 10, is more prominent in the multifluid model, where the separation of species allows for ions to flow in different directions.

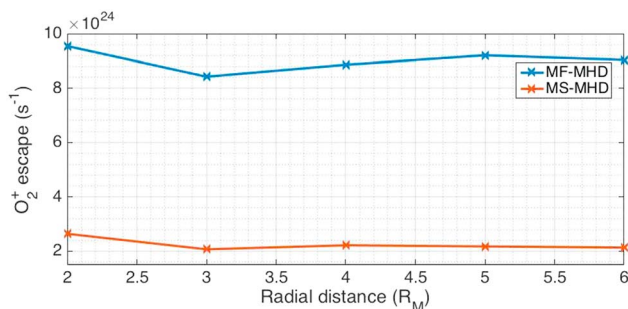


Figure 10. Outward O_2^+ fluxes as a function of radial distance. MS = multispecies; MF = multifluid; MHD = magnetohydrodynamic.

This result has direct implications for the measurements being carried out by orbiting spacecraft at Mars. The plot in Figure 10 suggests that, to get a clear picture of the outflow of heavy ions, measurements need to be taken at distances of at least 5 to $6R_M$ downstream of the planet. This implies that part of the outflow (up to about 10%) being detected by MAVEN (with an apoapsis distance of about $2R_M$) or Mars Express (with an apoapsis of just over $3R_M$) will eventually return to the planet. That being said, the variation is less than a factor of 2 so the effect is smaller than the uncertainties present due to spacecraft charging effects.

The above numbers show that, despite the uncertainties in the estimation of the escape, the models are producing results that compare to the data within at least an order of magnitude. This has been extensively reported in the literature (e.g., Dong et al., 2014; Ma et al., 2004). Given that the calculations based on STATIC data are expected to be an underestimate due to the lack of information on the low-energy part of the spectrum, the results provided by the multifluid model are expected to be closer to the actual escape rates.

Focusing on the two models, there are different factors that explain the different results. From the maps presented in Figure 5, the limitation of the multispecies approach when studying heavy ion escape becomes evident. Given that only one momentum equation is solved for all the ion species, the velocity distribution will be dominated by the ions carrying most of the momentum, that is, the solar wind protons. This makes it impossible for the model to capture any asymmetry in the escape channels such as the plume that arises from the escape of heavier particles.

For the reason just described, the totality of the escape in the multispecies model occurs at the center of the tail. In the case of the multifluid model, apart from the north-south asymmetry due to the specific direction of the solar wind convection electric field, there is a longitudinal asymmetry that increases with distance from the equator that has its cause in three asymmetries present in the simulations. These are the magnetic pressure arising from the B_x component of the IMF, the presence of the crustal fields and the distribution of densities in the neutral atmosphere.

Limitations of the current models. Apart from the return bulk flows, individual heavy ions can return to the planet due to finite gyroradius effects (in addition, a Marsward proton flux has been observed with MAVEN, although the reasons for this remains unclear; Harada, et al., 2015b). This is beyond the inherent capabilities of the MHD formulation and estimating the effects of this would require the use of a hybrid approach. In any case, since this would be caused by individual particles, it is expected that the overall effect will be smaller than that of the return bulk flow.

Recently, Brecht et al. (2017) analyzed the effect of the electron temperature in hybrid simulations. They found that different electron temperature profiles change the outflow rates by changing the strength of the induced ambipolar electric field. This field has been suggested as a possible ionospheric escape mechanism for all the bodies in the solar system, although the strength of the field is thought to be too small to be measured with current instrumentation (e.g., Coates et al., 2015; Fung & Hoffman, 1991). A recent study by Collinson et al. (2016) places the potential drop at Venus at a surprisingly high value of 10.6 V with important implications for heavy ion escape. In the current version of the MHD models, the electron temperature is assumed to be the same as the ion temperature, leading to underestimates of the ambipolar electric field strength.

Another factor that can affect the estimates of ion outflow from both simulation approaches presented in this study is the presence of plasma instabilities in the induced magnetosphere that can further complicate the escape trajectory of ions. The initial acceleration of ionospheric ions by the presence of the solar wind convection electric field introduces a temperature anisotropy in the form of a ring distribution unstable to the generation of ion cyclotron waves (e.g., Romanelli et al., 2013; Russell et al., 2006; Wei et al., 2011). This process is mass dependent, meaning that different ion species will evolve differently. Also, the difference in velocity of the different ion populations can lead to the development of two-stream instabilities that work toward limiting the difference in flow velocities (Glocer et al., 2009).

The physical presence of the two-stream instability would act to accelerate the ions flowing with lower speeds while decelerating those with higher speeds and thus increasing the total escape rate, so this limitation of the growth by the MHD approach introduces a further limiting factor for the estimates of ion escape. While this can be developed in the multifluid model, its effect has not been fully analyzed in the framework of the MHD simulations.

Acknowledgments

The authors would like to acknowledge the contributions of Y. Shou, G. Toth, and K. Klein for fruitful discussions during the development of this work. This work was supported by a NASA Living With a Star grant (NNX16AL12G). Simulations were run at the Pleiades supercomputer, part of the NASA Advanced Supercomputing Division, and the results are available in Regoli (2018). All MAVEN data are made publicly available through the NASA Planetary Data System.

References

- Arkani-Hamed, J. (2001). A 50-degree spherical harmonic model of the magnetic field of Mars. *Journal of Geophysical Research*, *106*, 23,197–23,208. <https://doi.org/10.1029/2000JE001365>
- Barabash, S., Fedorov, A., Lundin, R., & Sauvaud, J.-A. (2007). Martian atmospheric erosion rates. *Science*, *315*, 501–503. <https://doi.org/10.1126/science.1134358>
- Böswetter, A., Simon, S., Bagdonat, T., Motschmann, U., Fränz, M., Roussos, E., et al. (2007). Comparison of plasma data from ASPERA-3/Mars-Express with a 3-D hybrid simulation. *Annales Geophysicae*, *25*, 1851–1864. <https://doi.org/10.5194/angeo-25-1851-2007>
- Bougher, S. W., Engel, S., Roble, R. G., & Foster, B. (1999). Comparative terrestrial planet thermospheres 2. Solar cycle variation of global structure and winds at equinox. *Journal of Geophysical Research*, *104*, 16,591–16,611. <https://doi.org/10.1029/1998JE001019>
- Bougher, S. W., Pawlowski, D., Bell, J. M., Nelli, S., McDunn, T., Murphy, J. R., et al. (2015). Mars Global Ionosphere-Thermosphere Model: Solar cycle, seasonal, and diurnal variations of the Mars upper atmosphere. *Journal of Geophysical Research: Planets*, *120*, 311–342. <https://doi.org/10.1002/2014JE004715>
- Brain, D. A., Bagenal, F., Ma, Y.-J., Nilsson, H., & Stenberg Wieser, G. (2016). Atmospheric escape from unmagnetized bodies. *Journal of Geophysical Research: Planets*, *121*, 2364–2385. <https://doi.org/10.1002/2016JE005162>
- Brain, D. A., Hurley, D., & Combi, M. R. (2010). The solar wind interaction with Mars: Recent progress and future directions. *Icarus*, *206*(1), 1–4. <https://doi.org/10.1016/j.icarus.2009.10.020>
- Brain, D. A., Lillis, R. J., Mitchell, D. L., Halekas, J. S., & Lin, R. P. (2007). Electron pitch angle distributions as indicators of magnetic field topology near Mars. *Journal of Geophysical Research*, *112*, A09201. <https://doi.org/10.1029/2007JA012435>
- Brain, D. A., McFadden, J. P., Halekas, J. S., Connerney, J. E. P., Bougher, S. W., Curry, S., et al. (2015). The spatial distribution of planetary ion fluxes near Mars observed by MAVEN. *Geophysical Research Letters*, *42*, 9142–9148. <https://doi.org/10.1002/2015GL065293>
- Brecht, S. H., Ferrante, J. R., & Luhmann, J. G. (1993). Three-dimensional simulations of the solar wind interaction with Mars. *Journal of Geophysical Research*, *98*, 1345–1357. <https://doi.org/10.1029/92JA02198>
- Brecht, S. H., Ledvina, S. A., & Bougher, S. W. (2016). Ionospheric loss from Mars as predicted by hybrid particle simulations. *Journal of Geophysical Research: Space Physics*, *121*, 10,190–10,208. <https://doi.org/10.1002/2016JA022548>
- Brecht, S. H., Ledvina, S. A., & Jakosky, B. M. (2017). The role of the electron temperature on ion loss from Mars. *Journal of Geophysical Research: Space Physics*, *122*, 8375–8390. <https://doi.org/10.1002/2016JA023510>
- Cloutier, P. A., McElroy, M. B., & Michel, F. C. (1969). Modification of the Martian ionosphere by the solar wind. *Journal of Geophysical Research*, *74*, 6215. <https://doi.org/10.1029/JA074i026p06215>
- Coates, A. J., Wellbrock, A., Waite, J. H., & Jones, G. H. (2015). A new upper limit to the field-aligned potential near Titan. *Geophysical Research Letters*, *42*, 4676–4684. <https://doi.org/10.1002/2015GL064474>
- Collinson, G. A., Frahm, R. A., Glocer, A., Coates, A. J., Grebowsky, J. M., Barabash, S., et al. (2016). The electric wind of Venus: A global and persistent “polar wind”-like ambipolar electric field sufficient for the direct escape of heavy ionospheric ions. *Geophysical Research Letters*, *43*, 5926–5934. <https://doi.org/10.1002/2016GL068327>
- Dong, C., Bougher, S. W., Ma, Y., Toth, G., Lee, Y., Nagy, A. F., et al. (2015). Solar wind interaction with the Martian upper atmosphere: Crustal field orientation, solar cycle, and seasonal variations. *Journal of Geophysical Research: Space Physics*, *120*, 7857–7872. <https://doi.org/10.1002/2015JA020990>
- Dong, C., Bougher, S. W., Ma, Y., Toth, G., Nagy, A. F., & Najib, D. (2014). Solar wind interaction with Mars upper atmosphere: Results from the one-way coupling between the multifluid MHD model and the MTGCM model. *Geophysical Research Letters*, *41*, 2708–2715. <https://doi.org/10.1002/2014GL059515>
- Dong, Y., Fang, X., Brain, D. A., McFadden, J. P., Halekas, J. S., Connerney, J. E., et al. (2015). Strong plume fluxes at Mars observed by MAVEN: An important planetary ion escape channel. *Geophysical Research Letters*, *42*, 8942–8950. <https://doi.org/10.1002/2015GL065346>
- Dong, Y., Fang, X., Brain, D. A., McFadden, J. P., Halekas, J. S., Connerney, J. E. P., et al. (2017). Seasonal variability of Martian ion escape through the plume and tail from MAVEN observations. *Journal of Geophysical Research: Space Physics*, *122*, 4009–4022. <https://doi.org/10.1002/2016JA023517>
- Dubinin, E., Fraenz, M., Pätzold, M., McFadden, J., Halekas, J. S., DiBraccio, G. A., et al. (2017). The effect of solar wind variations on the escape of oxygen ions from Mars through different channels: MAVEN observations. *Journal of Geophysical Research: Space Physics*, *122*, 11,285–11,301. <https://doi.org/10.1002/2017JA024741>
- Dubinin, E., Fraenz, M., Pätzold, M., McFadden, J., Mahaffy, P. R., Eparvier, F., et al. (2017). “Effects of solar irradiance on the upper ionosphere and oxygen ion escape at Mars: MAVEN observations”. *Journal of Geophysical Research: Space Physics*, *122*, 7142–7152. <https://doi.org/10.1002/2017JA024126>
- Dubinin, E., Fraenz, M., Woch, J., Zhang, T. L., Wei, J., Fedorov, A., et al. (2012). Bursty escape fluxes in plasma sheets of Mars and Venus. *Geophysical Research Letters*, *39*, L01104. <https://doi.org/10.1029/2011GL049883>
- Dubinin, E., Fränz, M., Woch, J., Roussos, E., Barabash, S., Lundin, R., et al. (2006). Plasma Morphology at Mars. Aspera-3 Observations. *Space Science Reviews*, *126*, 209–238. <https://doi.org/10.1007/s11214-006-9039-4>
- Eastwood, J. P., Brain, D. A., Halekas, J. S., Drake, J. F., Phan, T. D., Øieroset, M., et al. (2008). Evidence for collisionless magnetic reconnection at Mars. *Geophysical Research Letters*, *35*, L02106. <https://doi.org/10.1029/2007GL032289>
- Fang, X., Ma, Y., Masunaga, K., Dong, Y., Brain, D., Halekas, J., et al. (2017). The Mars crustal magnetic field control of plasma boundary locations and atmospheric loss: MHD prediction and comparison with MAVEN. *Journal of Geophysical Research: Space Physics*, *122*, 4117–4137. <https://doi.org/10.1002/2016JA023509>
- Fjeldbo, G., & Eshleman, V. R. (1968). The atmosphere of Mars analyzed by integral inversion of the Mariner IV occultation data. *Planetary and Space Science*, *16*, 1035–1059. [https://doi.org/10.1016/0032-0633\(68\)90020-2](https://doi.org/10.1016/0032-0633(68)90020-2)
- Fox, J. L., & Hač, A. B. (2009). Photochemical escape of oxygen from Mars: A comparison of the exobase approximation to a Monte Carlo method. *Icarus*, *204*, 527–544. <https://doi.org/10.1016/j.icarus.2009.07.005>
- Fränz, M., Dubinin, E., Andrews, D., Barabash, S., Nilsson, H., & Fedorov, A. (2015). Cold ion escape from the Martian ionosphere. *Planetary and Space Science*, *119*, 92–102. <https://doi.org/10.1016/j.pss.2015.07.012>
- Fung, S. F., & Hoffman, R. A. (1991). A search for parallel electric fields by observing secondary electrons and photoelectrons in the low-altitude auroral zone. *Journal of Geophysical Research*, *96*, 3533–3548. <https://doi.org/10.1029/90JA02244>
- Glocer, A., Tóth, G., Ma, Y., Gombosi, T., Zhang, J.-C., & Kistler, L. M. (2009). Multifluid Block-Adaptive-Tree Solar wind Roe-type Upwind Scheme: Magnetospheric composition and dynamics during geomagnetic storms—Initial results. *Journal of Geophysical Research*, *114*, A12203. <https://doi.org/10.1029/2009JA014418>
- Halekas, J. S., Eastwood, J. P., Brain, D. A., Phan, T. D., Øieroset, M., & Lin, R. P. (2009). In situ observations of reconnection Hall magnetic fields at Mars: Evidence for ion diffusion region encounters. *Journal of Geophysical Research*, *114*, A11204. <https://doi.org/10.1029/2009JA014544>

- Harada, Y., Halekas, J. S., McFadden, J. P., Mitchell, D. L., Mazelle, C., Connerney, J. E. P., et al. (2015a). Magnetic reconnection in the near-Mars magnetotail: MAVEN observations. *Geophysical Research Letters*, *42*, 8838–8845. <https://doi.org/10.1002/2015GL065004>
- Harada, Y., Halekas, J. S., McFadden, J. P., Mitchell, D. L., Mazelle, C., Connerney, J. E. P., et al. (2015b). Marsward and tailward ions in the near-Mars magnetotail: MAVEN observations. *Geophysical Research Letters*, *42*, 8925–8932. <https://doi.org/10.1002/2015GL065005>
- Harnett, E. M., & Wingless, R. M. (2006). Three-dimensional multifluid simulations of ionospheric loss at Mars from nominal solar wind conditions to magnetic cloud events. *Journal of Geophysical Research*, *111*, A09213. <https://doi.org/10.1029/2006JA011724>
- Holmström, M., & Wang, X.-D. (2015). Mars as a comet: Solar wind interaction on a large scale. *Planetary and Space Science*, *119*, 43–47. <https://doi.org/10.1016/j.pss.2015.09.017>
- Jakosky, B. M., Lin, R. P., Grebowsky, J. M., Luhmann, J. G., Mitchell, D. F., Beutelschies, G., et al. (2015). The Mars Atmosphere and Volatile Evolution (MAVEN) Mission. *Space Science Reviews*, *195*, 3–48. <https://doi.org/10.1007/s11214-015-0139-x>
- Kallio, E., Fedorov, A., Budnik, E., Säles, T., Janhunen, P., Schmidt, W., et al. (2006). Ion escape at Mars: Comparison of a 3-D hybrid simulation with Mars Express IMA/ASPERA-3 measurements. *Icarus*, *182*, 350–359. <https://doi.org/10.1016/j.icarus.2005.09.018>
- Lammer, H., Chassefière, E., Karatekin, O., Morschhauser, A., Niles, P. B., Mousis, O., et al. (2013). Outgassing history and escape of the Martian atmosphere and water inventory. *Space Science Reviews*, *174*(1), 113–154.
- Ledvina, S. A., Ma, Y.-J., & Kallio, E. (2008). Modeling and simulating flowing plasmas and related phenomena. *Space Science Reviews*, *139*(1), 143–189. <https://doi.org/10.1007/s11214-008-9384-6>
- Lundin, R., Zakharov, A., Pellinen, R., Barabash, S. W., Borg, H., Dubinin, E. M., et al. (1990). Aspera/Phobos measurements of the ion outflow from the MARTIAN ionosphere. *Geophysical Research Letters*, *17*(6), 873–876.
- Lunine, J. I., Chambers, J., Morbidelli, A., & Leshin, L. A. (2003). The origin of water on Mars. *Icarus*, *165*(1), 1–8.
- Ma, Y., Fang, X., Russell, C. T., Nagy, A. F., Toth, G., Luhmann, J. G., et al. (2014). Effects of crustal field rotation on the solar wind plasma interaction with Mars. *Geophysical Research Letters*, *41*, 6563–6569. <https://doi.org/10.1002/2014GL060785>
- Ma, Y., Nagy, A. F., Sokolov, I. V., & Hansen, K. C. (2004). Three-dimensional, multispecies, high spatial resolution MHD studies of the solar wind interaction with Mars. *Journal of Geophysical Research*, *109*, A07211. <https://doi.org/10.1029/2003JA010367>
- McFadden, J. P., Kortmann, O., Curtis, D., Dalton, G., Johnson, G., Abiad, R., et al. (2015). MAVEN SupraThermal and Thermal Ion Composition (STATIC) instrument. *Space Science Reviews*, *195*, 199–256. <https://doi.org/10.1007/s11214-015-0175-6>
- Modolo, R., Chanteur, G. M., Dubinin, E., & Matthews, A. P. (2005). Influence of the solar EUV flux on the Martian plasma environment. *Annales Geophysicae*, *23*, 433–444. <https://doi.org/10.5194/angeo-23-433-2005>
- Najib, D., Nagy, A. F., Toth, G., & Ma, Y. (2011). Three-dimensional, multifluid, high spatial resolution MHD model studies of the solar wind interaction with Mars. *Journal of Geophysical Research*, *116*, A05204. <https://doi.org/10.1029/2010JA016272>
- Nilsson, H., Edberg, N. J. T., Stenberg, G., Barabash, S., Holmström, M., Futaana, Y., et al. (2011). Heavy ion escape from Mars, influence from solar wind conditions and crustal magnetic fields. *Icarus*, *215*, 475–484. <https://doi.org/10.1016/j.icarus.2011.08.003>
- Powell, K. G., Roe, P. L., Linde, T. J., Gombosi, T. I., & Zeeuw, D. L. D. (1999). A solution-adaptive upwind scheme for ideal magnetohydrodynamics. *Journal of Computational Physics*, *154*(2), 284–309. <https://doi.org/10.1006/jcph.1999.6299>
- Ramstad, R., Barabash, S., Futaana, Y., Nilsson, H., & Holmström, M. (2017). Global Mars—Solar wind coupling and ion escape. *Journal of Geophysical Research: Space Physics*, *122*, 8051–8062. <https://doi.org/10.1002/2017JA024306>
- Regoli, L. H. (2018). Simulation outputs for M-GITM, MS-MHD and MF-MHD. <https://doi.org/10.7302/Z2GH9G49>
- Romanelli, N., Bertucci, C., Gómez, D., Mazelle, C., & Delva, M. (2013). Proton cyclotron waves upstream from Mars: Observations from Mars Global Surveyor. *Planetary and Space Science*, *76*, 1–9. <https://doi.org/10.1016/j.pss.2012.10.011>
- Russell, C. T., Mayerberger, S. S., & Blanco-Cano, X. (2006). Proton cyclotron waves at Mars and Venus. *Advances in Space Research*, *38*, 745–751. <https://doi.org/10.1016/j.asr.2005.02.091>
- Verigin, M. I., Shutte, N. M., Galeev, A. A., Gringauz, K. I., Kotova, G. A., Remizov, A. P., et al. (1991). Ions of planetary origin in the Martian magnetosphere (Phobos 2/TAUS experiment). *Planetary and Space Science*, *39*, 131–137. [https://doi.org/10.1016/0032-0633\(91\)90135-W](https://doi.org/10.1016/0032-0633(91)90135-W)
- Wei, H. Y., Russell, C. T., Zhang, T. L., & Blanco-Cano, X. (2011). Comparative study of ion cyclotron waves at Mars, Venus and Earth. *Planetary and Space Science*, *59*, 1039–1047. <https://doi.org/10.1016/j.pss.2010.01.004>